









Spectral splitting of a stimulated Raman transition in a single molecule

Johannes Zirkelbach ^{1,2,*} Burak Gurlek ^{1,2,†} Masoud Mirzaei ^{1,2} Alexey Shkarin ¹ Tobias Utikal ¹
Stephan Götzinger ^{2,1,3} and Vahid Sandoghdar ^{1,2,‡}

¹Max Planck Institute for the Science of Light, D-91058 Erlangen, Germany

²Department of Physics, Friedrich-Alexander-University Erlangen Nürnberg, D-91058 Erlangen, Germany

³Graduate School in Advanced Optical Technologies (SAOT), Friedrich-Alexander University Erlangen-Nürnberg, D-91052 Erlangen, Germany

 (Received 28 February 2023; revised 11 July 2023; accepted 5 November 2023; published 14 December 2023)

The small cross-section of Raman scattering poses a great challenge for its direct study at the single-molecule level. By exploiting the high Franck-Condon factor of a common-mode resonance, choosing a large vibrational frequency difference in electronic ground and excited states and operating at $T < 2$ K, we succeed at driving a coherent stimulated Raman transition in individual molecules. We observe and model a spectral splitting that serves as a characteristic signature of the phenomenon at hand. Our study sets the ground for exploiting the intrinsic optomechanical degrees of freedom of molecules for applications in solid-state quantum optics and information processing.

DOI: [10.1103/PhysRevResearch.5.043244](https://doi.org/10.1103/PhysRevResearch.5.043244)

I. INTRODUCTION

On February 28, 1928, C. V. Raman recorded spectra that provided conclusive evidence for inelastic coherent scattering in the optical domain [1,2]. Today, we know that the Raman process is due to the coupling of the atomic vibrations in a molecule to its electronic transitions, which can be seen as the natural realization of a quantum optomechanical phenomenon [3–5]. The effect has found a wide-spread interest for its molecular fingerprinting capacity in sensing and diagnostics applications [6,7]. These investigations typically involve ensembles of molecules since cross-sections of Raman scattering are extremely small, although single-molecule sensitivity has been reported in schemes based on near-field plasmonic enhancement [4,8–12]. In a recent study, Xiong *et al.* achieved single-molecule Raman microscopy with chemical sensitivity at room temperature using a clever electronically preresonant stimulated Raman scheme [13]. In this paper, we demonstrate robust single-molecule Raman signals obtained at high spectral resolution in a coherent and fully resonant configuration under cryogenic conditions.

In 1989, Moerner and Kador showed that single polycyclic aromatic hydrocarbons (PAHs) embedded in crystalline matrices could be addressed at liquid helium temperature via

Fourier-limited zero-phonon lines (00ZPL) connecting the vibrational ground levels of the electronic ground and excited states [14]. Since then, a wide range of optical experiments have exploited the 00ZPLs of PAHs for quantum optical and nonlinear optical investigations [15–18]. However, the vibrational levels of the electronic states have only been studied via incoherent spectroscopy in these systems [19–22]. In what follows, we show that despite short lifetimes of the order of picoseconds, it is possible to drive resonant stimulated Raman transitions to vibrational levels of the electronic ground state using continuous-wave (CW) laser radiation, leading to the observation of spectral splitting. This work paves the way for coherent quantum optical operations using the vibrational degrees of freedom in molecules.

II. COHERENCE AND SPECTRAL SPLITTING IN MULTI-LEVEL QUANTUM SYSTEMS

We begin with a brief theoretical discussion of the interaction between two laser fields and a generic four-level molecule [13,23–26], in line with other treatments in the broader context of coherent optical processes such as electromagnetically induced transparency (EIT) and Autler-Townes splitting (ATS) [27–29]. Figure 1(a) depicts the general level scheme, where $|g\rangle$ and $|e\rangle$ denote the molecular electronic ground and excited states, respectively, with no vibrational excitation. States $|v\rangle$ and $|w\rangle$ stand for their vibrational levels with much shorter lifetimes due to rapid phonon-assisted relaxation in the solid matrix [30–32]. Parameters Γ_i represent the decay rate of state $|i\rangle$, whereby in our system $\Gamma_w \approx 2\Gamma_v \gg \Gamma_e$.

In the rotating-wave approximation, the Hamiltonian of the model system can be written as [28]

$$\hat{H} = \hbar \begin{pmatrix} 0 & 0 & \Omega_{ge}/2 & \Omega_{exc}/2 \\ 0 & \Delta_{stk} - \Delta_{exc} & 0 & \Omega_{stk}/2 \\ \Omega_{ge}/2 & 0 & -\Delta_{ge} & 0 \\ \Omega_{exc}/2 & \Omega_{stk}/2 & 0 & -\Delta_{exc} \end{pmatrix} \quad (1)$$

*Current address: Faculty of Physics, Ludwig-Maximilians-Universität München, D-85748 Garching, Germany.

†Current address: Max Planck Institute for the Structure and Dynamics of Matter and Center for Free-Electron Laser Science, D-22761 Hamburg, Germany.

‡vahid.sandoghdar@mpl.mpg.de

Published by the American Physical Society under the terms of the Creative Commons Attribution 4.0 International license. Further distribution of this work must maintain attribution to the author(s) and the published article's title, journal citation, and DOI. Open access publication funded by the Max Planck Society.

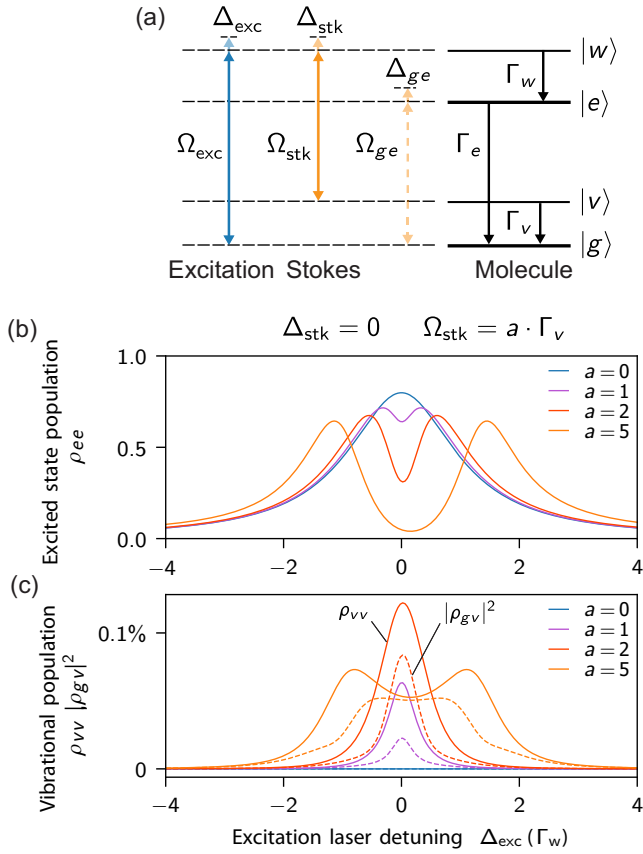


FIG. 1. (a) Level scheme for model calculations including the electronic ground and excited states $|g\rangle$ and $|e\rangle$ with no vibrational excitation as well as the vibronic states $|v\rangle$ and $|w\rangle$. Arrows indicate which transitions can be reached with the excitation laser (blue) and Stokes laser (orange). Γ_i : Relaxation rates, Ω_i : Rabi frequencies, Δ_i : frequency detunings. (b) Population in state $|e\rangle$ for $\Gamma_w = 2\Gamma_v = 1000\Gamma_e$, $\Omega_{\text{exc}} = 2\sqrt{\Gamma_e\Gamma_w}$, $(\nu_{vw} - \nu_{ge})/(2\pi) = -10\Gamma_w$, $\Omega_{ge} = \Omega_{\text{stk}}$, $\Delta_{\text{stk}} = 0$, and various values of the Stokes laser Rabi frequency $\Omega_{\text{stk}} = a \cdot \Gamma_v$. The values are plotted as a function of the excitation laser detuning Δ_{exc} . For $\Omega_{\text{stk}} = 5\Gamma_v$, the profile is not centered around $\Delta_{\text{exc}} = 0$ because the Stokes laser exerts a noticeable AC-Stark shift on the $|g\rangle \leftrightarrow |e\rangle$ transition. (c) Same as in (b) but for ρ_{vv} (solid curves) and its coherent part $|\rho_{gv}|^2$ (dashed curves).

in the rotating frame with the basis $\{|g\rangle, |v\rangle, |e\rangle, |w\rangle\}$. Here, $\Omega_{\text{exc}} = -\vec{d}_{gv} \cdot \vec{E}_{\text{exc}}/\hbar$ and $\Omega_{\text{stk}} = -\vec{d}_{vw} \cdot \vec{E}_{\text{stk}}/\hbar$ denote the Rabi frequencies produced by the excitation (exc) and Stokes (stk) laser fields, \vec{E}_{exc} and \vec{E}_{stk} , respectively, and \vec{d}_{ij} is the transition dipole moment between states $|i\rangle$ and $|j\rangle$. In addition, $\Omega_{ge} = \beta_g \Omega_{\text{stk}}$, where $\beta_g = \|\vec{d}_{ge}\|/\|\vec{d}_{vw}\|$ represents the relative Franck-Condon (FC) overlap between the 00ZPL and the $|v\rangle \leftrightarrow |w\rangle$ transition. We have included the $|g\rangle \leftrightarrow |e\rangle$ transition in the model because of its spectral vicinity to the $|w\rangle \leftrightarrow |v\rangle$ transition addressed by the Stokes laser. The parameters $\Delta_{\text{exc}} = 2\pi(\nu_{\text{exc}} - \nu_{gw})$, $\Delta_{\text{stk}} = 2\pi(\nu_{\text{stk}} - \nu_{vw})$ and $\Delta_{ge} = 2\pi(\nu_{\text{stk}} - \nu_{ge})$ signify various frequency detunings. Here, ν_{ij} stands for the frequency of the $|i\rangle \leftrightarrow |j\rangle$ transition, and ν_{exc} and ν_{stk} are the frequencies of the excitation and Stokes lasers, respectively (see Appendixes B and C). From

a quantum optical perspective, such a system is situated between the EIT and ATS regimes for moderate driving of the $|v\rangle \leftrightarrow |w\rangle$ transition ($\Omega_{\text{stk}} \lesssim \Gamma_w$) [33–35].

Considering that $|w\rangle$ decays very fast, the population ρ_{ee} of $|e\rangle$ reports on the excitation of the molecule via the $|g\rangle \leftrightarrow |w\rangle$ transition. In Fig. 1(b), we portray the numerical solution of the Lindblad master equation for ρ_{ee} . These spectral profiles result from a line splitting and a dip that forms in the absorption profile of the transition $|g\rangle \leftrightarrow |w\rangle$ as coherent population exchange via the vibronic $|w\rangle \leftrightarrow |v\rangle$ transition becomes comparable to the relaxation rate of $|v\rangle$ and $|w\rangle$, i.e., as Ω_{stk} becomes comparable to Γ_v, Γ_w . Indeed, ρ_{ww} follows the same spectral profile as ρ_{ee} , albeit with a much smaller amplitude. The quantities ρ_{vv} (solid curves) and $|\rho_{gv}|^2$ (dashed curves) in Fig. 1(c) show that a small fraction of the population is coherently transferred to $|v\rangle$, establishing a stimulated Raman transition from $|g\rangle$ to $|v\rangle$. The correspondence between the spectral profiles of ρ_{vv} and ρ_{ee} , which is in turn directly proportional to the fluorescence signal, provides a convenient metric for the occurrence of a Raman transition, which we exploit in our experiment.

III. EXPERIMENTAL SCHEME

The measurements in this work were performed on dibenzoterrylene (DBT: $\text{C}_{38}\text{H}_{20}$) embedded in a paradichlorobenzene (pDCB: $\text{C}_6\text{H}_4\text{Cl}_2$) crystal [36] at a molar concentration of 30 ppb [see Fig. 2(a)]. As sketched in Fig. 2(b), the doped pDCB crystal was formed in a channel of sub-micrometer depth created between a fused silica substrate and a solid-immersion lens (refractive index $n = 2.14$) [16,37]. This configuration allowed efficient coupling of two focused laser beams to DBT molecules in the sample. We remark that we chose the DBT doping level to be low enough to find no more than one molecule in the excitation volume. Second-order autocorrelation measurements of the molecular fluorescence confirmed that the signals presented in this study stem from a single molecule (see [22]). Experiments were performed in a closed-cycle dilution refrigerator that operated at a base temperature of $T \sim 25$ mK (see Appendix A).

In Fig. 2(c), we display the energy levels of the most prominent vibronic transitions associated with the electronic ground (S_0) and excited (S_1) states of a molecule according to the experimentally recorded data presented on the right-hand side of the figure [22]. The linewidth of the 00ZPL connecting the electronic ground state $|g\rangle$ to the electronic excited state $|e\rangle$ with no vibrational excitation corresponds to $\Gamma_e/(2\pi) = 23$ MHz. The linewidths of $|v\rangle$ and $|w\rangle$ were measured to be $\Gamma_v/(2\pi) = 13.5$ GHz and $\Gamma_w/(2\pi) = 26.1$ GHz via fluorescence excitation and stimulated emission depletion (STED), respectively (see Ref. [22] and Appendix E). In order to drive a coherent Raman process, the beams of two independently tunable and narrowband (linewidth < 100 kHz) Ti:sapphire lasers were overlapped and coupled to a confocal microscope (see Appendix A). In contrast to our previous work about incoherent vibronic spectroscopy [22], this latter scheme enables coherent processes since both lasers were tuned to transitions from the *same* upper quantum state.

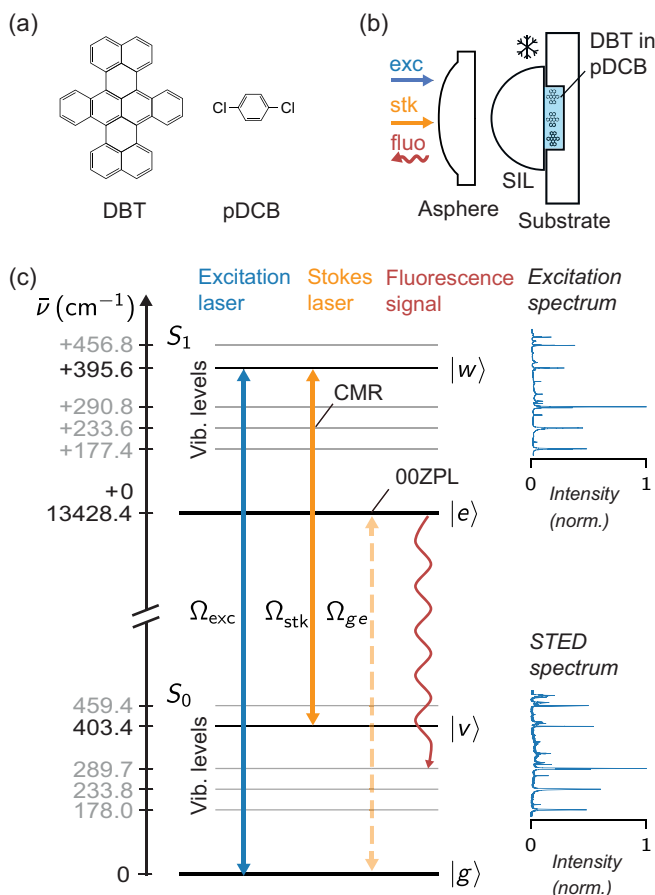


FIG. 2. (a) Chemical structures of DBT and pDCB. (b) Sketch of the sample and focusing optics in the cryostat. Exc: excitation laser, stk: Stokes laser, fluo: fluorescence, SIL: solid-immersion lens. (c) Level scheme of a DBT molecule with several vibronic states associated with the most prominent vibronic transitions from the vibrational ground states $|g\rangle$ and $|e\rangle$. Transitions $|g\rangle \leftrightarrow |w\rangle$ and $|v\rangle \leftrightarrow |w\rangle$ addressed by the two lasers are marked by solid double-headed arrows. The dashed double-headed arrow indicates that the Stokes laser is in the spectral vicinity of the 00ZPL transition. The curvy red arrow indicates the fluorescence transition used to measure the molecular excited state population. CMR: common mode resonance.

To optimize the efficiency of coherent transitions, it is desirable to work with high FC factors and low Γ_i . In molecules with a prominent 00ZPL (such as DBT), common mode resonances (CMR: electronic transitions conserving the vibrational quantum numbers [38]) tend to have the highest FC factors (see Appendix B). Moreover, it is favorable to choose a pair of vibronic states in S_0 and S_1 with a transition frequency that is considerably detuned from the 00ZPL to satisfy $\Omega_{ge} \ll \Delta_{ge}$ in order to minimize the probability of exciting $|e\rangle$ by the Stokes laser. We selected the CMR between the modes close to 400 cm^{-1} with a detuning of about 232 GHz from the 00ZPL. The response of the molecule was monitored via the red-shifted fluorescence on a prominent transition from $|e\rangle$ to a vibronic level in S_0 at about 290 cm^{-1} (width of bandpass filter: 2 nm).

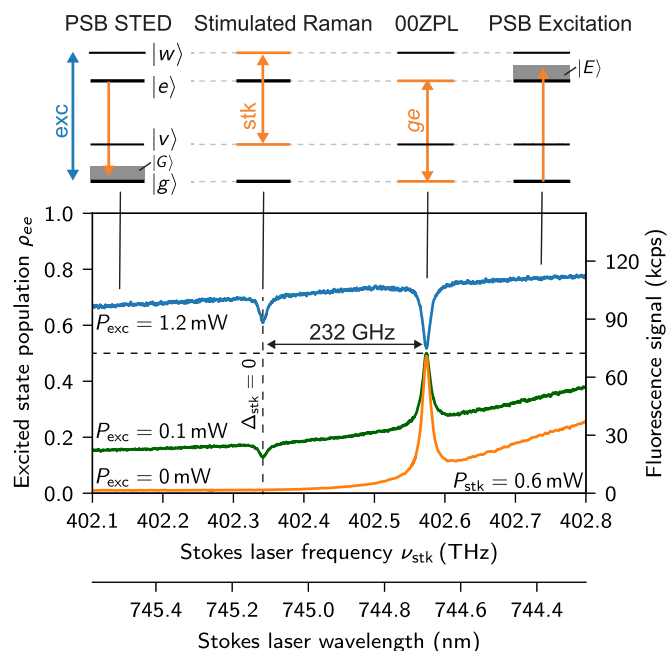


FIG. 3. Scan of the Stokes laser frequency ν_{stk} at various power levels of the resonant excitation laser ($\Delta_{\text{exc}} = 0$). The level schemes on top of the plot indicate the processes underlying the spectral features in the data. PSB: phonon sideband, STED: stimulated emission depletion, 00ZPL: 00-zero-phonon line.

IV. EXPERIMENTAL RESULTS

A. Identification of the Raman transition

The spectra in Fig. 3 show the background-corrected fluorescence signal R_{fluo} and $\rho_{ee} = R_{\text{fluo}}/R_{\infty}$ deduced from it as ν_{stk} was scanned, while ν_{exc} was set on the resonance of the $|g\rangle \leftrightarrow |w\rangle$ transition (R_{∞} denotes the fluorescence count rate at full saturation; see Appendix D). The scan range was chosen to cover both the 00ZPL and $|v\rangle \leftrightarrow |w\rangle$ transition frequencies. Three exemplary spectra taken at different excitation powers represent the cases of negative and positive population inversion between $|g\rangle$ and $|e\rangle$. The level schemes in the upper part of the figure illustrate the different transitions that contribute to the various parts of the spectrum. In the case of $P_{\text{exc}} = 0$ (orange), we observe a peak when the Stokes laser is resonant with the 00ZPL. The slope of the base line in the region where $\nu_{\text{stk}} \gtrsim \nu_{ge}$ is caused by excitation via the tail of the phonon side band (PSB) in $|e\rangle$ (denoted by $|E\rangle$) [39,40]. As the excitation power is increased (green), more population is transferred from $|g\rangle$ to $|e\rangle$ via $|w\rangle$ and a larger fluorescence signal is generated, leading to a higher base line. On the Raman resonance ($\Delta_{\text{stk}} = \Delta_{\text{exc}} = 0$), the coherence induced between $|w\rangle$ and $|v\rangle$ leads to a dip in the fluorescence profile and the transfer of population to $|v\rangle$. At very large excitation powers ($P_{\text{exc}} = 1.2\text{ mW}$, blue), ρ_{ee} exceeds ρ_{gg} such that the Stokes laser can stimulate transitions back to $|g\rangle$, resulting in a dip at the 00ZPL frequency. At $P_{\text{exc}} = 0.1\text{ mW}$ and $P_{\text{exc}} = 1.2\text{ mW}$, the (slight) drop in the fluorescence signal for $\nu_{\text{stk}} \lesssim 402.4\text{ THz}$ is related to stimulated emission from $|e\rangle$ to the PSB of $|g\rangle$ (denoted $|G\rangle$).

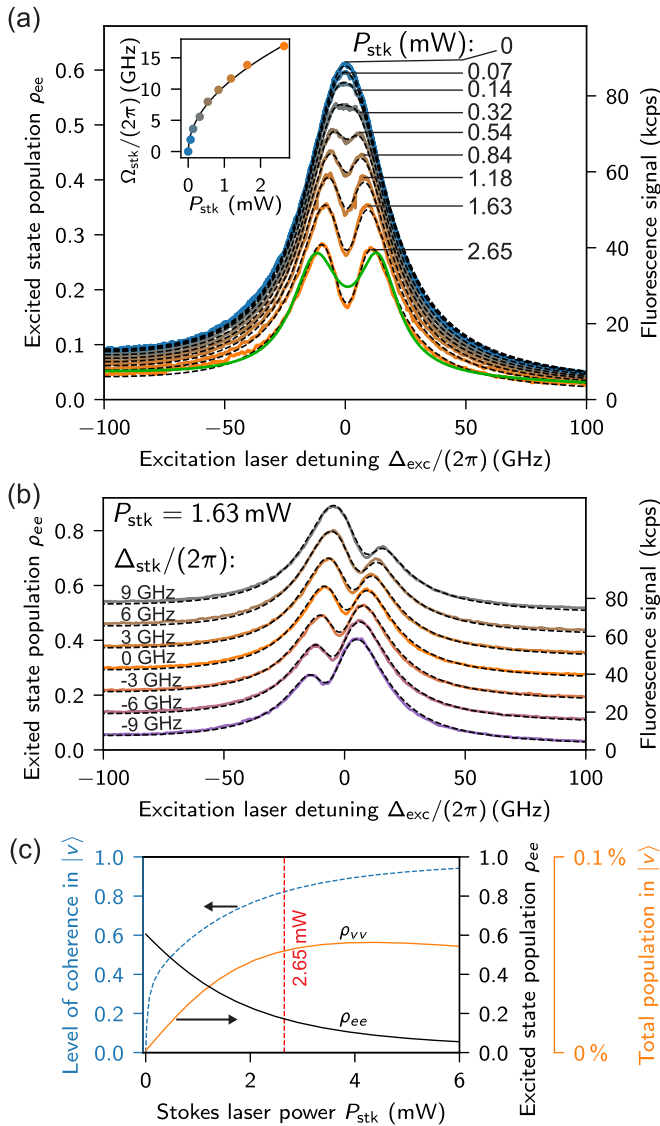


FIG. 4. Resonant stimulated Raman transition in a single DBT molecule. (a) Excitation spectra of the vibronic transition $|g\rangle \leftrightarrow |w\rangle$ monitored via fluorescence from $|e\rangle$ as a function of the excitation laser frequency detuning (Δ_{exc}). Spectra were recorded at different powers (P_{stk}) of the Stokes laser at $\Delta_{stk} = 0$ and $P_{exc} = 0.6$ mW ($\Omega_{exc} = \sqrt{1.5}\Gamma_e\Gamma_w$). Green curve depicts a fit to the sum of two Lorentzian functions. (b) Same as in (a) but for different Δ_{stk} and at $P_{stk} = 1.63$ mW. The data are plotted with an offset. (c) Total populations ρ_{vv} (solid orange line) and ρ_{ee} (solid black line), and level of coherence in $|v\rangle$ ($|\rho_{gv}|^2/\rho_{vv}$, dashed blue line) at $\Delta_{exc} = 0$ as predicted by the model fitted to the data in (a).

B. Spectral splitting in the resonant Raman configuration

Next, we fixed the frequency of the Stokes laser to the CMR ($\Delta_{stk} = 0$), set $P_{exc} = 0.6$ mW (corresponding to $\Omega_{exc} \approx \sqrt{1.5}\Gamma_e\Gamma_w$) and scanned ν_{exc} through the resonance of the $|g\rangle \leftrightarrow |w\rangle$ transition. The outcome of these measurements is presented for various P_{stk} in Fig. 4(a) (see Appendix D for background correction applied to the data). It is evident that as predicted in Fig. 1(b), the original Lorentzian line profile develops a dip for larger P_{stk} values. This dip corresponds to

the inverse band shapes encountered in conventional resonant stimulated Raman spectroscopy [23–26,41].

To compare our experimental data with theoretical expectations, the model presented in Fig. 1 was modified to include energy transfer to the crystal via $|G\rangle$ and $|E\rangle$ as well as an additional vibronic transition to a level $|x\rangle$ close to $|w\rangle$ (see Appendix C). The black lines in Fig. 4(a) show the results of the model fit to the data, whereby only Ω_{stk} and $\beta_G = \|\vec{d}_{Ge}\|/\|\vec{d}_{vw}\|$ acted as free parameters. All remaining quantities were independently determined from STED spectroscopy [22] and a fluorescence excitation scan in the absence of the Stokes laser (see Appendix E). As expected, we find that Ω_{stk} scales with $\sqrt{P_{stk}}$ [see inset in Fig. 4(a)]. The drops in the fluorescence amplitude and baseline are caused by stimulated depletion of the excited state into $|G\rangle$ (see Secs. C and E of the Appendix). We remark the observed dip cannot be attributed to an ATS process as the spectral profile clearly deviates from a fit to the sum of two Lorentzians [see the green curve in Fig. 4(a)] [33–35].

We also performed a similar experiment while varying the Stokes frequency detunings around the CMR at a fixed Stokes laser power ($P_{stk} = 1.63$ mW). The outcome is presented in Fig. 4(b) and reports a smooth shift of the induced dip over the spectral profile of the $|g\rangle \leftrightarrow |w\rangle$ transition. The dashed curves display the result of the theoretical model, which is in excellent agreement with the measured data without any additional free fit parameters.

C. Vibrational coherence

In Fig. 4(c), we plot the predictions of the model for populations ρ_{vv} (orange curve) and ρ_{ee} (black curve) when $\Delta_{exc} = \Delta_{stk} = 0$ (see Appendix F). The blue dashed line presents the degree of coherence $|\rho_{gv}|^2/\rho_{vv}$ obtained from the fit to the data of Fig. 4(a). The model states that for the maximum power $P_{stk} = 2.65$ mW used in our experiment (red dashed line), approximately 80% of the population that is transferred to $|v\rangle$ undergoes a coherent process (see Appendix D). In other words, the molecular vibrations have a fixed phase relation with the beating oscillations of the two driving lasers. This phenomenon is analogous to the coherence of scattering from a laser-driven two-level atom [42]. We also find that the level of coherence transferred to $|v\rangle$ increases with P_{stk} as the laser-mediated transfer becomes faster than Γ_v and Γ_w . Moreover, ρ_{vv} drops again with increasing P_{stk} due to the emergence of a line splitting. Since $|v\rangle$ relaxes within ~ 10 ps, the steady-state population in this level remains limited to $\rho_{vv} < 10^{-3}$ in the experimental scheme employed here.

V. THEORETICAL PREDICTIONS FOR HIGHER LASER POWERS

To elucidate the wider parameter space that can be explored, we present the vibrational population ρ_{vv} and its coherent part $|\rho_{gv}|^2$ as a function of Ω_{exc} , Ω_{stk} , and Δ_{exc} in Fig. 5. The red crosses and dashed lines mark the parameters of this work. The data in Figs. 5(a) and 5(c) show that on resonance, a considerably more efficient population transfer could take place if one increased the excitation power by about 25 times. In Figs. 5(b) and 5(d), we study the effect of frequency

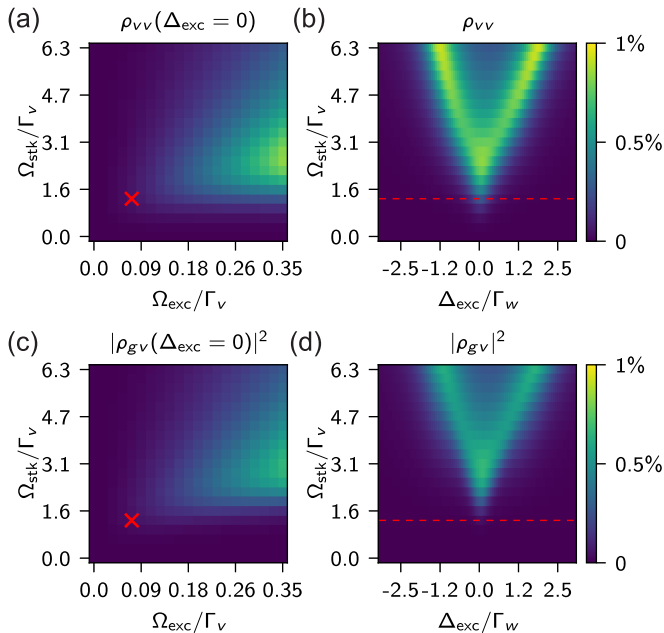


FIG. 5. Theoretical predictions for total (a,b) and coherent (c,d) population in $|v\rangle$ for various combinations of the excitation and Stokes laser Rabi frequencies (Ω_{exc} and Ω_{stk}) as well as the excitation laser frequency detuning. $\Delta_{\text{stk}} = 0$ for all cases. The red markers and lines indicate the (maximum) values used in our experiments.

detuning away from resonance, emphasizing that due to the splitting caused by the coherent interaction, the optimal Raman transition does not take place at the original resonance condition $\Delta_{\text{exc}} = 0$. Furthermore, Fig. 5(b) shows the regime, where a population transfer as large as 1% to state $|v\rangle$ can be achieved (of which 60% is coherent), corresponding to an efficient vibrational Raman process in a molecular system.

VI. CONCLUSION

In conclusion, we studied the laser-induced coherent line splitting associated with a stimulated Raman transition in a single organic molecule embedded in a crystal. Background fluorescence was minimized by probing a higher-lying vibrational level that does not directly fluoresce at the detection wavelength. Furthermore, the Stokes laser was tuned to a common mode resonance with a high FC factor to compete with the fast relaxation rates of the vibronic states in the solid state. By using tight focusing at cryogenic temperatures, the Raman transition could be achieved at CW laser powers as low as 1 mW.

Our study paves the way for a number of future investigations. For example, the observed line splitting can be used to infer the absolute transition dipole moments of vibronic transitions if a thorough intensity calibration of the optical focus is performed [43,44]. Furthermore, one can study the Raman effect in single molecules in a quantitative fashion and in close comparison with theoretical models, e.g., as one tunes the transition from resonance to far off resonance conditions [23,24,45]. Moreover, the rich manifolds of electronic and vibrational energy levels in molecules [46–50] could be explored for achieving coherent population transfer and storage

for applications in quantum information processing, similar to schemes such as STIRAP [51] or EIT [27,52–56].

ACKNOWLEDGMENTS

We thank Irena Deperasińska and Boleslaw Kozankiewicz for fruitful discussions and for sharing the results of their DFT calculations with us. We also thank Jan Renger for fabricating the nanochannels.

B.G. and M.M. contributed equally to this work. This research was funded by the Max Planck Society.

APPENDIX A: SAMPLE PREPARATION AND EXPERIMENTAL SETUP

The data presented in the main text were recorded using a single dibenzoterrylene (DBT) molecule in a para-dichlorobenzene (pDCB) crystal at cryogenic temperatures. This molecule was part of a sample used to demonstrate high-resolution STED spectroscopy and its vibronic properties are discussed in detail in [22] (*molecule 1 on sample 3*, as defined in the supplementary material of [22]). A thorough description of the sample preparation and the experimental setup can be found in the supplementary material of [22] and in [57]. We remark that line splitting effects equivalent to those reported in the main text could also be reproduced with other DBT molecules on various samples of DBT in pDCB.

We melted a DBT-doped pDCB crystal with a (low) nominal molar doping level of 30 ppb and introduced it into a 460 nm deep nanochannel formed between a SiO_2 substrate and a hemispherical solid immersion lens (SIL; ZrO_2 ; AWI Industries; $n = 2.14$) with a radius of 1.5 mm. The high-index solid immersion lens improves the light-molecule interaction by focusing the light to a tighter diffraction-limited spot. In this configuration, we were able to address single DBT molecules by spatial selection because we found on average not more than one DBT molecule per focal volume.

For our experiment and all measurements described in this study, the sample was stored in a dilution refrigerator that reaches a base temperature of $T \sim 25$ mK [57]. A pronounced antibunching dip in the autocorrelation traces of the molecular fluorescence measured in this configuration verifies that it stems from a single molecule [22]. Autocorrelation measurements additionally reveal that the triplet yield and lifetime for the molecule under study were $\phi = 3 \times 10^{-6}$ and $1/\Gamma_{I_g} = 40$ μs , respectively. The related autocorrelation measurements are provided in Ref. [22]. As a consequence, the population accumulated in the triplet remains negligible ($< 0.5\%$) at the temperatures of our experiment, even if saturation of the optical transition is reached (see also Ref. [36] for more details on the photophysical properties of DBT in pDCB).

Figure 6 shows a sketch of the optical setup used for the experiment described in the main text. The optical setup corresponds to a confocal microscope for addressing single DBT molecules in the cryostat. The light of two narrow-band, tunable, and intensity-stabilized Ti:sapphire lasers is coupled to the (same) beam path of the microscope. The laser light reflected from the sample is blocked by a suitable bandpass filter (realized by several tunable long and shortpass filters) in the detection path to isolate and detect the fluorescence

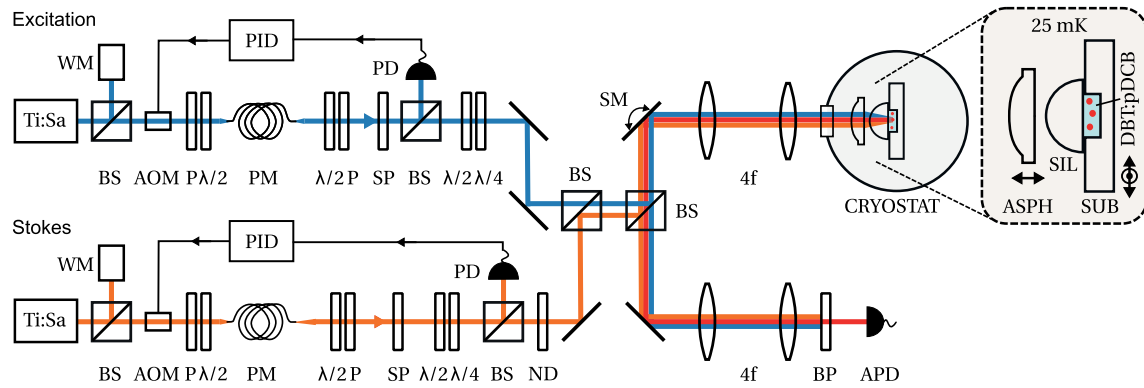


FIG. 6. Sketch of the experimental setup. Abbreviations: 4f: 4f telecentric system – AOM: acousto-optic modulator – APD: avalanche photodiode – ASPH: aspheric lens – BP: bandpass filter – BS: beam splitter – CRYOSTAT: dilution cryostat – $\lambda/2$: half-wave plate – $\lambda/4$: quarter-wave plate – ND: variable neutral density filter – PD: photodiode – PID: PID-controller – PM: polarization-maintaining fiber – P: linear polarizer – SIL: solid immersion lens – SM: scanning mirror – SP: shortpass filter – SUB: substrate with etched nano-channel – Ti:Sa: tunable Ti:sapphire laser – WM: wavemeter.

from the molecule with an avalanche photodiode (APD). In contrast to the experimental arrangement in Ref. [22], the ~ 2 nm wide transmission window of the bandpass filter is set to ~ 393.9 THz (761.7 nm) corresponding to the most prominent fluorescent vibronic transition from the electronically excited state of the molecule. The emission of the 00ZPL was not used for detection due to the difficulty of filtering out the intense Stokes laser close to resonant with the strongest transition in the molecule. We remark that the data presented in the main text are obtained without intensity modulation of the excitation or Stokes laser. Moreover, there was no need to adjust their temporal synchronization since they operated in the continuous-wave mode.

APPENDIX B: NOTATION

We use $|S_0\rangle$ and $|S_1\rangle$ to denote the electronic ground and first excited singlet states, respectively, and $|\bar{\nu}\rangle$ to denote a

vibronic state of DBT with vibrational wavenumber $\bar{\nu}$. The direct product $|S_k, \bar{\nu}\rangle = |S_k\rangle|\bar{\nu}\rangle$ (with $k \in \{0, 1\}$) is a vibronic state. Vibrational ground states are denoted by $|S_k, 0\rangle$.

The 00ZPL is the transition between the vibrational ground states $|S_0, 0\rangle$ and $|S_1, 0\rangle$. A *vibronic* transition is a transition between vibronic states that involves a change in the electronic quantum number. In the Franck-Condon (FC) approximation, the transition dipole moment of the vibronic transition between $|S_0, \bar{\nu}\rangle$ and $|S_1, \bar{\nu}'\rangle$ is proportional to its FC factor $|\langle \bar{\nu} | \bar{\nu}' \rangle|^2$. Methods for calculating FC factors of polyatomic molecules can be found in [58,59]. We refer to the transition between a fundamental vibration in S_0 and its counterpart mode in S_1 (i.e., the mode with the most similar displacement vectors) as *common mode resonance* (CMR) [38]. DFT calculations [60] indicate that for (almost) all states $|S_k, \bar{\nu}\rangle$ of DBT the transition dipole moment of the CMR exceeds the transition dipole moments of all other vibronic transitions.

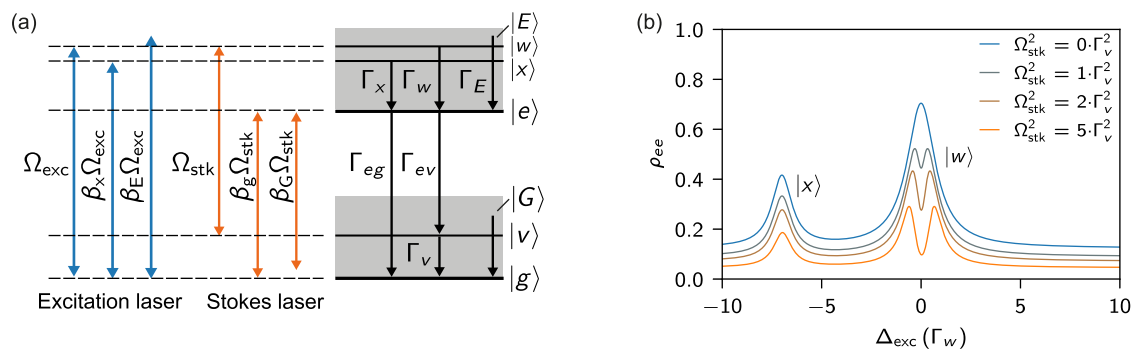


FIG. 7. Model used to fit the experimental data. (a) Level scheme including seven molecular states and their spontaneous decay rates as well as several laser-induced transitions. The states $|g\rangle$, $|v\rangle$, $|e\rangle$, and $|w\rangle$ correspond to those used in Fig. 2 of the main text. $|G\rangle$ and $|E\rangle$ are phonon sideband ‘states’ and $|x\rangle$ is an additional vibronic level in the spectral vicinity of $|w\rangle$. (b) Vibronic line profile of the transitions $|g\rangle \leftrightarrow |w\rangle$ and $|g\rangle \leftrightarrow |x\rangle$ for various values of the Stokes laser Rabi frequency and model parameters that resemble the experimental data: $\Delta_{\text{stk}} = 0$, $\Gamma_w/(2\pi) = 25$ GHz, $\Gamma_x = \Gamma_E = \Gamma_w$, $\Gamma_v = \Gamma_w/2$, $\Gamma_e/(2\pi) = \Gamma_{eg}/(2\pi) = 23$ MHz, $\Gamma_{ev} = 0$, $\Gamma_G = 1/(1 \text{ ps})$, $\delta_{gw, gx} = 7 \cdot \Gamma_w$, $\delta_{vw, ge} = -10 \cdot \Gamma_w$, $\Omega_{\text{exc}}^2/(\Gamma_e \Gamma_w) = 1.5$, $\beta_E = 0.25$, $\beta_x = 0.5$, $\beta_g = 1$, and $\beta_G = 0.1$. The model assumes that the FC factor of the transition $|v\rangle \leftrightarrow |x\rangle$ vanishes. As the Stokes laser Rabi frequency increases, the line profile of $|w\rangle$ splits and the amplitude of the spectral profile of $|w\rangle$ as well as the background level decrease due to stimulated emission along $|e\rangle \rightarrow |G\rangle$.

Additionally, we use the following shorthand notation for the most relevant molecular states in the context of our experiment:

$ g\rangle = S_0, 0\rangle$	vibrational ground state of the electronic ground state,
$ v\rangle = S_0, 403.4 \text{ cm}^{-1}\rangle$	fundamental vibration of the mode measured at $\bar{\nu} = 403.4 \text{ cm}^{-1}$ in the electronic ground state,
$ e\rangle = S_1, 0\rangle$,	vibrational ground state of the electronic excited state,
$ w\rangle = S_1, 395.6 \text{ cm}^{-1}\rangle$	fundamental vibration of the mode at $\bar{\nu} = 395.6 \text{ cm}^{-1}$ in the electronically excited state. The vibrational pattern of this mode corresponds to the one of the mode at 403.4 cm^{-1} in S_0 .

The total (spontaneous) decay rate of state $|i\rangle$ is denoted by Γ_i .

APPENDIX C: MODEL FOR VIBRONIC LINE SPLITTING OF A MOLECULE IN A SOLID

Energy transfer to the matrix leads to phonon sidebands associated with transitions in molecules in the solid [39,61]. These spectrally broad PSBs are indicated schematically by the gray areas in the level scheme displayed in Fig. 7(a). For a full explanation of our experimental data on spectral splitting, transitions to PSBs need to be included into the model. Moreover, we also consider the transition to a vibronic level in the spectral vicinity of $|w\rangle$.

Figure 7(a) shows the full model used to fit the experimental data in Fig. 4 in the main manuscript. The three levels and transitions that are not part of the energy level scheme shown in Fig. 1 of the main manuscript are

(1) $|G\rangle$: phonon sideband of $|g\rangle$; describes the depletion of $|e\rangle$ via stimulated emission along $|e\rangle \rightarrow |G\rangle$ triggered by the Stokes laser.

(2) $|x\rangle$: vibronic level in the spectral vicinity of the probed level $|w\rangle$; required because the tail of the transition $|g\rangle \leftrightarrow |x\rangle$ slightly overlaps with the spectral profile of the transition $|g\rangle \leftrightarrow |w\rangle$ [see also Fig. 9(c)].

(3) $|E\rangle$: PSB of vibronic levels and combination modes in S_1 ; describes the absorption of the excitation laser by the molecule which is not associated with transitions to $|w\rangle$ or $|x\rangle$.

To simulate the behavior of the model described in the manuscript, we applied the rotating wave approximation and transformed the system to a suitable rotating frame in which the Hamiltonian has no explicit time-dependence. Then we used *QuTiP* [62] to determine the excited state population $\rho_{ee} = |e\rangle\langle e|$ as a function of the Rabi frequencies and detunings of the excitation laser and the Stokes laser, respectively.

In the basis $I = \{|g\rangle, |G\rangle, |v\rangle, |e\rangle, |E\rangle, |w\rangle, |x\rangle\}$, the Hamiltonian used for the *QuTiP*-simulations is:

$$\hat{H} = \hbar \begin{pmatrix} 0 & 0 & 0 & \beta_g \Omega_{\text{stk}}/2 & \beta_E \Omega_{\text{exc}}/2 & \Omega_{\text{exc}}/2 & \beta_x \Omega_{\text{exc}}/2 \\ 0 & -\Delta_{\text{stk}} - \delta_{vw,ge} & 0 & \beta_G \Omega_{\text{stk}}/2 & 0 & 0 & 0 \\ 0 & 0 & \Delta_{\text{stk}} - \Delta_{\text{exc}} & 0 & 0 & \Omega_{\text{stk}}/2 & 0 \\ \beta_g \Omega_{\text{stk}}/2 & \beta_G \Omega_{\text{stk}}/2 & 0 & -\Delta_{\text{stk}} - \delta_{vw,ge} & 0 & 0 & 0 \\ \beta_E \Omega_{\text{exc}}/2 & 0 & 0 & 0 & 0 & 0 & 0 \\ \Omega_{\text{exc}}/2 & 0 & \Omega_{\text{stk}}/2 & 0 & 0 & -\Delta_{\text{exc}} & 0 \\ \beta_x \Omega_{\text{exc}}/2 & 0 & 0 & 0 & 0 & 0 & -\Delta_{\text{exc}} - \delta_{gw,gx} \end{pmatrix}. \quad (\text{C1})$$

Here, we used the notation $\Delta_{\text{exc}} = \omega_{\text{exc}} - \omega_{gw}$ for the detuning of the excitation laser, $\Delta_{\text{stk}} = \omega_{\text{stk}} - \omega_{vw}$ for the detuning of the Stokes laser (as defined in the main text), $\delta_{gw,ge} = \omega_{gw} - \omega_{ge}$, $\delta_{vw,ge} = \omega_{vw} - \omega_{ge}$, and $\delta_{gw,gx} = \omega_{gw} - \omega_{gx}$. The parameters ω_{exc} and ω_{stk} denote the (angular) frequencies of the excitation and Stokes lasers, respectively, and ω_{ij} denotes the (angular) frequency of the transition between states $|i\rangle$ and $|j\rangle$. As usual, the angular frequencies ω are related to the laser and transition frequencies ν via $\omega = 2\pi\nu$.

The steps and notation used for the derivation of Hamiltonian (C1) are as follows: the molecular Hamiltonian is given by $\hat{H}_m = \hbar \sum_{i \in I} \omega_i |i\rangle\langle i|$ and the molecule-field

Hamiltonian in the dipole approximation is $\hat{H}_{\text{mf}} = -\hat{d} \cdot \vec{E}(t)$ with the dipole operator $\hat{d} = \sum_{i,j \in I} |i\rangle\langle i| \hat{d}_{ij} |j\rangle\langle j|$ and the time-dependent electric field $\vec{E}(t) = \vec{E}_{\text{exc}} \cos(\omega_{\text{exc}} t) + \vec{E}_{\text{stk}} \cos(\omega_{\text{stk}} t)$, where \vec{E}_{exc} and \vec{E}_{stk} are the electric field vectors of the excitation and Stokes lasers at the position of the molecule, respectively. We assume that the phases used in the calculation of the transition dipole moments $\langle i| \hat{d}_{ij} |j\rangle$ are chosen such that the result for the transition dipole vector is real valued.

In a first step, the molecular Hamiltonian is transformed to the interaction picture via: $\hat{H}_I = \hat{U} \hat{H}_{\text{mf}} \hat{U}^\dagger$ with $\hat{U} = e^{i\hat{H}_m t/\hbar}$.

Then the RWA is applied by expressing the cosines in the electric field term $\vec{E}(t)$ using complex exponential functions, and only retaining terms that are close to resonance, i.e. terms containing $\omega_{\text{exc}} - \omega_{gw}$, $\omega_{\text{exc}} - \omega_{gx}$, $\omega_{\text{exc}} - \omega_{gE}$, $\omega_{\text{stk}} - \omega_{vw}$, $\omega_{\text{stk}} - \omega_{ge}$, and $\omega_{\text{stk}} - \omega_{gG}$. In the next step, the system is transformed back to the Schrödinger picture and the Rabi frequencies $\hbar\Omega_{\text{exc}} = -\vec{d}_{gw} \cdot \vec{E}_{\text{exc}}$, $\hbar\beta_x\Omega_{\text{exc}} = -\vec{d}_{gx} \cdot \vec{E}_{\text{exc}}$, $\hbar\beta_E\Omega_{\text{exc}} = -\vec{d}_{gE} \cdot \vec{E}_{\text{exc}}$, $\hbar\Omega_{\text{stk}} = -\vec{d}_{vw} \cdot \vec{E}_{\text{stk}}$, $\hbar\beta_g\Omega_{\text{stk}} = -\vec{d}_{ge} \cdot \vec{E}_{\text{stk}}$, and $\hbar\beta_G\Omega_{\text{stk}} = -\vec{d}_{gG} \cdot \vec{E}_{\text{stk}}$ are introduced.

Using

$$\tilde{H} = \exp(-i\hat{R})(\hat{H}_m + \hat{H}_{\text{RWA}})\exp(i\hat{R}) + \hbar\partial_t\hat{R} \quad (\text{C2})$$

with

$$\hat{R} = \text{diag}(4\omega_{\text{exc}}t/7, 4\omega_{\text{exc}}t/7, (\omega_{\text{stk}} - 3\omega_{\text{exc}}/7)t, (-\omega_{\text{stk}} + 4\omega_{\text{exc}}/7)t, -3\omega_{\text{exc}}t/7, -3\omega_{\text{exc}}t/7, -3\omega_{\text{exc}}t/7), \quad (\text{C3})$$

the system can then be transformed to a frame without time-dependencies in the Hamiltonian. The matrix \hat{R} was determined using the methods described in [63]. Subtracting $\hbar(\omega_g + 4\omega_{\text{exc}}/7)$ from the diagonal as well as setting $\omega_{gG} \rightarrow -\Delta_{\text{stk}} - \delta_{vw,ge}$ and $-\Delta_{\text{exc}} - \delta_{gw,gE} \rightarrow 0$ to let the PSB states follow the laser frequencies (i.e. have the resonance condition always fulfilled) yields the final Hamiltonian shown in equation (C1) (see also Ref. [57] for a more detailed derivation).

Figure 7(b) shows the excited state population resulting from the *QuTiP* simulations of the Lindblad master equation for the density matrix operator $\hat{\rho}$:

$$\partial_t\hat{\rho} = -\frac{i}{\hbar}[\hat{H}, \hat{\rho}] + \sum_k \Gamma_k \left(\hat{L}_k \hat{\rho} \hat{L}_k^\dagger - \frac{1}{2}(\hat{L}_k^\dagger \hat{L}_k \hat{\rho} + \hat{\rho} \hat{L}_k^\dagger \hat{L}_k) \right), \quad (\text{C4})$$

with the Hamiltonian (C1) and the Lindblad jump operators \hat{L}_k of the decay processes shown in Fig. 7(a). The parameters used for this model are listed in the caption of Fig. 7 and create a similar line profile as observed in our experiments. The background absorption and the additional state $|x\rangle$ are not present in the four-level model discussed in the main text. Moreover, the drop in the amplitude of the vibronic transitions as well as the drop in background intensity with increasing Stokes laser power are due to excited state depletion via $|e\rangle \rightarrow |G\rangle$. These are important ingredients for a complete description of our experimental observations.

We note that the derivation of the Hamiltonian of equation (1) in the main text follows the same steps. In this case, the matrix

$$\hat{R} = \frac{1}{2} \begin{pmatrix} \omega_{\text{exc}}t & 0 & 0 & 0 \\ 0 & (2\omega_{\text{stk}} - \omega_{\text{exc}})t & 0 & 0 \\ 0 & 0 & (\omega_{\text{exc}} - 2\omega_{\text{stk}})t & 0 \\ 0 & 0 & 0 & -\omega_{\text{exc}}t \end{pmatrix} \quad (\text{C5})$$

was used to transform to the rotating frame.

We note that the density matrix description discussed above is necessary to describe the coherent interaction between the simultaneously driven transitions $|g\rangle \leftrightarrow |w\rangle$ and $|v\rangle \leftrightarrow |w\rangle$ and the resulting dip in the fluorescence profile of $|g\rangle \leftrightarrow |w\rangle$. A rate equation approach as in our previous study

on incoherent vibronic spectroscopy [22] is not sufficient to model this effect.

APPENDIX D: BACKGROUND CORRECTION AND ESTIMATION OF EXCITED-STATE POPULATION

To estimate the excited state population ρ_{ee} from the fluorescence count rate, we determined the APD count rate R_∞ corresponding to full saturation of the vibronic transition $|g\rangle \leftrightarrow |w\rangle$. For this purpose, we tuned the excitation laser on resonance with the prominent vibronic transition from $|g\rangle$ to the level at around 291 cm^{-1} in S_1 [see Fig. 8(a)]. We chose this prominent vibronic transition over the transition to the probed state at 395.6 cm^{-1} because this allows us to reach higher maximum saturation parameters for a given value of the maximum laser power. The saturation scan was performed using the same settings of the detection bandpass filter as used in the splitting experiment in Fig. 4 of the main text. In this setting, only the fluorescence emitted in a narrow ($\sim 2 \text{ nm}$) spectral range around the emission along the prominent transition $|e\rangle \rightarrow |S_0, 290 \text{ cm}^{-1}\rangle$ was transmitted to the APD while light from the excitation laser reflected from the sample was blocked. A fit to the data in Fig. 8(a) results in $R_\infty = 145 \text{ kcps}$ for this configuration. We assume that this value also holds for the transition $|g\rangle \leftrightarrow |w\rangle$ since the decay of the vibrational states is about three orders of magnitude faster than the electronic decay in our system, leading to very similar values of the maximum reachable excited state population.

Figure 8(b) shows the raw data associated with the measurement displayed in Fig. 4(a) of the main manuscript. While the excitation laser beam ($P_{\text{exc}} = 0.58 \text{ mW}$) had a negligible contribution to the background within the narrow spectral range transmitted through the bandpass, the Stokes laser beam induced a noticeable background count rate R_{stk} on the APD. Figure 8(c) shows the APD count rate R_{stk} , recorded at various powers of the Stokes laser (resonant with the transition $|v\rangle \leftrightarrow |w\rangle$, i.e., for $\nu_{\text{stk}} = 402341.5 \text{ GHz}$) traversing the sample when the excitation laser was blocked ($P_{\text{exc}} = 0$). The dashed line in Fig. 8(c) is a linear fit to the data points with $P_{\text{stk}} \leq 0.1 \text{ mW}$. We are not sure what causes the super-linear increase of R_{stk} . One option is Stokes laser-mediated excitation of the molecule via transitions from thermally populated phonon states of the molecular ground state to the excited state $|e\rangle$ (i.e., the phonon wing feature visible at lower energies than the 00ZPL transition in Fig. 3 of the main text).

To estimate the excited state population ρ_{ee} , we first subtract R_{stk} from the raw APD signal R and then divide the result by R_∞ :

$$\rho_{ee} \approx (R - R_{\text{stk}})/R_\infty. \quad (\text{D1})$$

We remark that if R_{stk} is (partially) caused by fluorescence emission from the molecule, the resulting value of ρ_{ee} will deviate from the actual excited state population. Since the saturation parameter S_{0w} of the transition $|g\rangle \leftrightarrow |w\rangle$ driven by the excitation laser is small ($S_{0w} \lesssim 1.5$) during the measurement shown in Fig. 8(b), the transition is still close to the linear regime and the deviation of ρ_{ee} resulting from equation (D1) corresponds (approximately) to the population transferred via the Stokes laser from the electronic ground state to the electronic excited state. Removing these

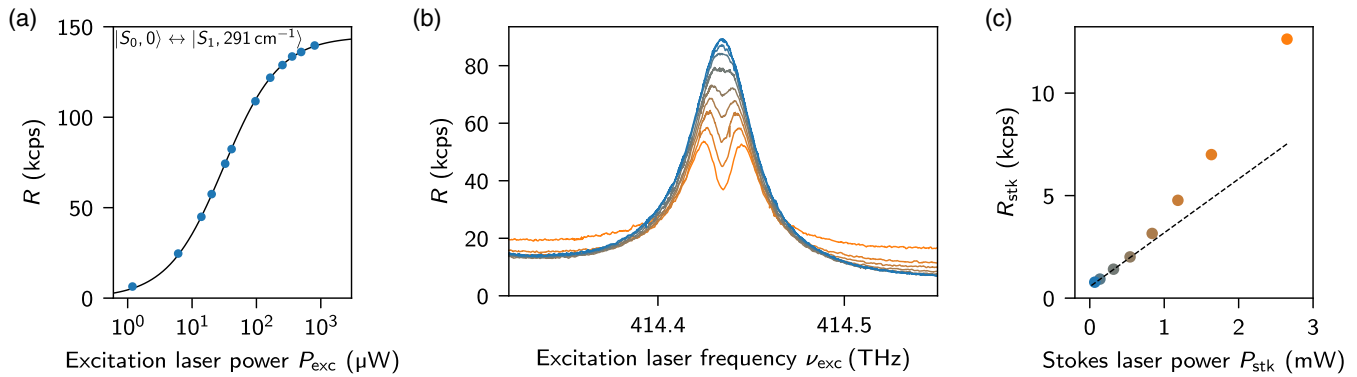


FIG. 8. (a) Saturation measurement of the prominent vibronic transition $|S_0, 0\rangle \leftrightarrow |S_1, 291 \text{ cm}^{-1}\rangle$ in S_1 (laser frequency: $\nu_{\text{exc}} = 411290 \text{ GHz}$). R denotes the count rate registered at the APD in the detection path (see Fig. 6). The measurement was performed on resonance with the vibronic transition and with the same settings of the detection bandpass as used for the vibronic splitting experiments. The fit of the function $R_\infty P/P_{\text{sat}}/(1 + P/P_{\text{sat}})$ yields $R_\infty = 145 \text{ kcps}$. (b) Raw APD count rate associated with the data shown in Fig. 4(a) of the main text. The colors indicate different powers of the Stokes laser as specified in (c). (c) Raw APD count rate recorded while the excitation laser was blocked and the Stokes laser was tuned on resonance with the transition $|v\rangle \leftrightarrow |w\rangle$. The dashed line is a linear fit to data points with $P_{\text{stk}} \leq 0.1 \text{ mW}$. The offset at $P_{\text{stk}} = 0$ is due to the dark counts of the APD and background stray light.

contributions via subtraction of the background has the advantage that Stokes-laser induced excitation of the molecule does not need to be included in the model. This reduces the number of free parameters in the model so that the Stokes laser only induces a population transfer from S_1 to S_0 via stimulated emission along $|e\rangle \rightarrow |G\rangle$. We also remark that equation (D1) requires $\rho_{ee}(S_{0w} \rightarrow \infty) \approx 1$, which is fulfilled for DBT due to the fast vibrational relaxation and low triplet yield.

APPENDIX E: MODEL FITTING

To fit the model described in Appendix C to the data, we minimized the number of free parameters by determining several fit parameters independently. The remaining free model parameters were determined from a fit of the *QuTiP* results for ρ_{ee} to the data obtained from the splitting measurements.

Table I provides an overview of the parameters used in this study and how they were determined.

1. Excited state $|e\rangle$: 00ZPL frequency and decay rate

The frequency of the 00ZPL of the molecule under investigation was $\omega_{ge}/(2\pi) = 402573.8 \text{ GHz}$ (744.689 nm). The decay rate Γ_e of the excited state can be determined via the linewidth of the 00ZPL transition in the low-excitation regime since dephasing is negligible in this system. As shown in more detail in Refs. [22,57], we obtained $\Gamma_e/(2\pi) = 22.8 \text{ MHz}$ ($4.2 \times 10^{-5} \text{ nm}$) from such a measurement and confirmed that this value was lifetime-limited using a pulsed measurement, which yielded a fluorescence lifetime of $\tau = 7 \text{ ns}$.

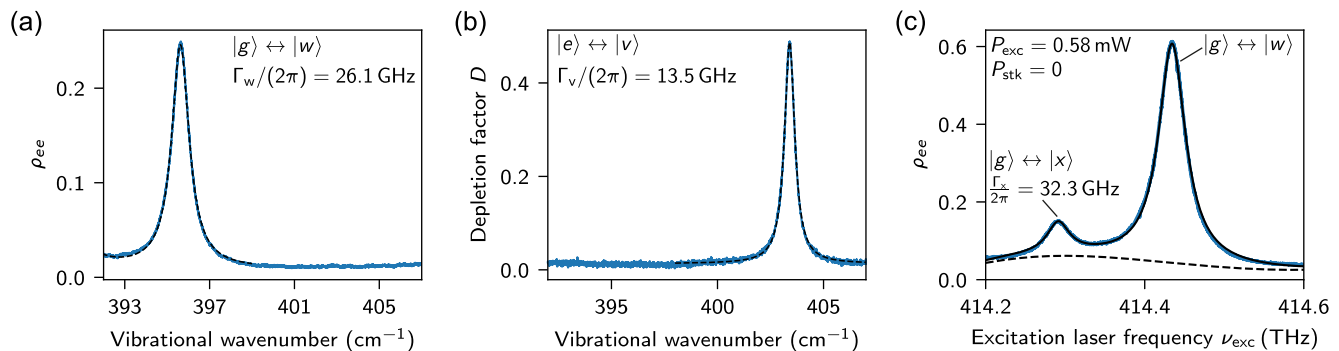


FIG. 9. Measurements for the independent determination of the parameters of the model shown in Fig. 7(a). (a) Fluorescence excitation scan of the transition $|g\rangle \leftrightarrow |w\rangle$. The black dashed line shows the fit of a rate equation model to the data (see Ref. [22] for more details). (b) STED spectroscopy measurement of the transition $|e\rangle \leftrightarrow |v\rangle$. The black dashed line shows the fit of a rate equation model to the data (see [22] for more details). A comparison of (a) and (b) shows that the vibrational wave number of the mode(s) associated with $|w\rangle$ and $|v\rangle$ is considerably higher in S_0 . (c) Scan of the excitation laser over the resonances of the transitions $|g\rangle \leftrightarrow |w\rangle$ and $|g\rangle \leftrightarrow |x\rangle$ under the same experimental conditions used to record the data of Figs. 8 and 4 (main text) and $P_{\text{stk}} = 0$. The solid black line shows a fit of ρ_{ee} resulting from a Lindblad master equation model using the Hamiltonian (C1). The black dashed line shows the ‘background’ absorption via level $|E\rangle$. See Appendix E3 for more details. We remark that (c) shows a similar scan as (a) but with a broader spectral range and a larger saturation parameter.

TABLE I. Summary of the parameters used in the model described in Appendix C. Most of the parameter values were obtained via independent measurements.

Parameter	Symbol	Value	Obtained via:
Electronic transition:			
$ g\rangle \leftrightarrow e\rangle$ transition freq.	$\omega_{ge}/(2\pi)$	402573.8 GHz	Fluorescence excitation scan [22]
Excited state decay rate	$\Gamma_e/(2\pi)$	22.8 MHz	Fluorescence excitation scan and pulsed autocorrelation measurement [22]
Population in $ e\rangle$	ρ_{ee}	<i>variable</i>	Fluorescence signal (see Appendix D)
Vibronic levels:			
$ g\rangle \leftrightarrow w\rangle$ transition freq.	$\omega_{gw}/(2\pi)$	414434.3 GHz	Fluorescence excitation scan [22]
Vib. decay rate (in $ e\rangle$)	$\Gamma_w/(2\pi)$	26.1 GHz	Fluorescence excitation scan [22]
Vibrational frequency (in $ e\rangle$)	$\omega_{ew}/(2\pi)$	11860.4 GHz	$(\omega_{gw} - \omega_{ge})/(2\pi)$
Excitation Rabi frequency	$\Omega_{exc}/(2\pi)$	0.95 GHz	Saturation scan of $ g\rangle \leftrightarrow w\rangle$ (Appendix D)
$ v\rangle \leftrightarrow e\rangle$ transition freq.	$\omega_{ve}/(2\pi)$	390480.6 GHz	STED spectroscopy [22]
Vib. decay rate (in $ g\rangle$)	$\Gamma_v/(2\pi)$	13.5 GHz	STED spectroscopy [22]
Vibrational frequency (in $ g\rangle$)	$\omega_{gv}/(2\pi)$	12093.2 GHz	$(\omega_{ge} - \omega_{ve})/(2\pi)$
Detuning	$\delta_{vw,ge}$	-232.7 GHz	$(\omega_{vw} - \omega_{ge})/(2\pi)$
Stokes Rabi frequency	$\Omega_{stk}/(2\pi)$	<i>variable</i>	Fit; see Fig. 4(a) of main text
Rel. transition dipole	β_g	1	Assuming that the FC factors of CMR & 00ZPL are equal (suggested by DFT simulations); the fit results are almost identical for $\beta_g = 0$
Population in $ v\rangle$	ρ_{vv}	<i>variable</i>	Fitted density matrix (this study)
Coherence between $ g\rangle$ and $ e\rangle$	ρ_{gv}	<i>variable</i>	Fitted density matrix (this study)
Phonon sidebands:			
Decay rate (in $ e\rangle$)	Γ_E	1/(1 ps)	Assuming fast decay
Rel. transition dipole	$\langle\beta_E\rangle$	0.17	Fluorescence excitation scan (average value; see Appendix E3)
Decay rate (in $ g\rangle$)	Γ_G	1/(1 ps)	Assuming fast decay
Rel. transition dipole	β_G	0.13	Fit (see Appendix E4)
Additional level:			
$ g\rangle \leftrightarrow x\rangle$ transition freq.	$\omega_{gx}/(2\pi)$	414291.3 GHz	Fluorescence excitation scan (Appendix E3)
Detuning	$\delta_{gw,gx}$	143.0 GHz	$(\omega_{gw} - \omega_{gx})/(2\pi)$
Vib. decay rate (in $ e\rangle$)	$\Gamma_x/(2\pi)$	32.3 GHz	Fluorescence excitation scan (Appendix E3)
Rel. transition dipole	β_x	0.29	Fluorescence excitation scan (Appendix E3)
Figures 4(c) and 5:			
Spontaneous decay to $ v\rangle$	Γ_{ev}	$0.01 \cdot \Gamma_{eg}$	Assumption inspired by DFT calculations. Reflects small incoherent contribution from spontaneous $ e\rangle \rightarrow v\rangle$ transitions

2. Vibronic states $|w\rangle$ and $|v\rangle$: frequencies and (vibrational) relaxation rates

The vibrational relaxation rates of $|w\rangle$ (at $\bar{\nu}_w \approx 395.6 \text{ cm}^{-1}$ in S_1) and $|v\rangle$ (at $\bar{\nu}_v \approx 403.4 \text{ cm}^{-1}$ in S_0) were determined using fluorescence excitation and STED spectroscopy measurements, respectively [22]. Figures 9(a) and 9(b) show the corresponding spectral profiles and fits of a rate equation model that corrects for power broadening effects and yields the lifetime-limited widths $\Gamma_w/(2\pi) = 26.1 \text{ GHz}$ ($4.6 \times 10^{-2} \text{ nm}$) and $\Gamma_v/(2\pi) = 13.5 \text{ GHz}$ ($2.7 \times 10^{-2} \text{ nm}$) of the associated transitions. The depletion factor D in STED spectroscopy is defined as $(\rho_{ee}(P_{stk} = 0) - \rho_{ee}(P_{stk})) / \rho_{ee}(P_{stk} = 0)$. See Refs. [22,57] for more details about these measurement methods and the associated modeling.

3. Probed transition $|g\rangle \leftrightarrow |w\rangle$

Figure 9(c) shows the probed spectral profile of the transitions $|g\rangle \leftrightarrow |w\rangle$ and $|g\rangle \leftrightarrow |x\rangle$ measured while the

Stokes laser was blocked ($P_{stk} = 0$) and using the excitation laser power that was set to the same value as the one used for the measurements shown in Fig. 4(a) of the main text. From a fit of ρ_{ee} resulting from *QuTiP* simulations of the Lindblad master equation for the Hamiltonian (C1) and the Lindblad decay terms for the decay processes indicated in Fig. 7(a), we obtained the parameters $\Gamma_x/(2\pi) = 32.3 \text{ GHz}$ ($5.6 \times 10^{-2} \text{ nm}$), $S_{0w} = \Omega_{exc}^2 / (\Gamma_e \Gamma_w) = 1.5$, $\beta_x = 0.29$, and $\omega_{gx}/(2\pi) = 414291.3 \text{ GHz}$ (723.627 nm). To capture the (slow) variation in absorption by PSBs and weak vibrational (combination) modes in S_1 , we allowed β_E to vary like a third-order polynomial as a function of excitation laser frequency. The resulting level of population ρ_{ee} transferred to the excited state via $|g\rangle \leftrightarrow |E\rangle$ is shown as a dashed line in Fig. 9(c).

For the fit to the data in Fig. 4(a) of the main text, the parameters ω_{ge} and Γ_e from Appendix E1 and the parameters ω_{gw} , Γ_w , ω_{gv} , and Γ_v from Appendix E2 were used as fixed fit parameters. We also assumed $\Gamma_E = \Gamma_w$, since we have no direct access to the lifetimes of the PSB and combination modes

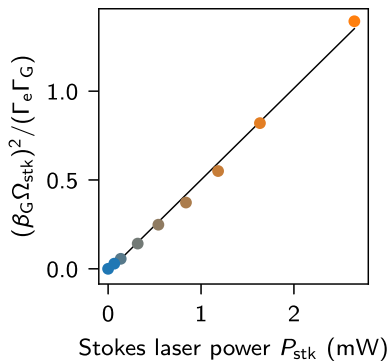


FIG. 10. Saturation parameter of the excited state depletion process via $|e\rangle \leftrightarrow |G\rangle$ resulting from the fit of the model discussed in Appendix C to the data of Fig. 4(a) in the main text. The black line is a linear fit to the data points.

around $|w\rangle$. Furthermore, we assumed fast relaxation of $|G\rangle$, i.e., $1/\Gamma_G = 1$ ps. This assumption guarantees fast depopulation of $|G\rangle$. Note that the exact value of Γ_G cannot be easily determined and is not relevant for the behavior of the model. The physically relevant quantity in the context of transitions to state $|G\rangle$ is $(\beta_G \Omega_{\text{stk}})^2 / (\Gamma_e \Gamma_G)$, which corresponds to the saturation parameter of the excited state depletion via transitions $|e\rangle \rightarrow |G\rangle$ driven by the Stokes laser. See Appendix E 4 for the behavior of this saturation parameter as a function of Stokes laser power P_{stk} .

4. Saturation parameter of excited state depletion via $|e\rangle \leftrightarrow |G\rangle$

Figure 10 shows the fit results for the saturation parameter of excited state depletion via the Stokes laser in the course of the splitting measurements presented in Fig. 4(a) of the main text. The outcome of the fit for β_G and Ω_{stk} used in this plot was obtained from the model described in Appendix C to the data of Fig. 4(a) in the main manuscript. As expected, the saturation parameter $(\beta_G \Omega_{\text{stk}})^2 / (\Gamma_e \Gamma_G)$ increases linearly with laser power.

APPENDIX F: LEVEL OF COHERENCE IN THE VIBRONIC POPULATION ρ_{vv}

In the configuration described for Fig. 1 of the main text (or Fig. 7 in the Appendix), the level $|v\rangle$ is excited via the pathways $|g\rangle \rightarrow |w\rangle \rightarrow |v\rangle$ and $|g\rangle \rightarrow |w\rangle \rightarrow |e\rangle \rightarrow |v\rangle$. While coherence with the driving laser fields is destroyed for the latter pathway due to the spontaneous decay processes $|w\rangle \rightarrow |e\rangle$ and $|e\rangle \rightarrow |v\rangle$, it can be transferred to $|v\rangle$ via the two simultaneously driven transitions of the former pathway. We note that this process is also only partly coherent as incoherent contributions become prominent as a transition is driven more closely to saturation. One can quantify the level of coherence in $\hat{\rho}_{vv} = \hat{\sigma}_{gv}^\dagger \hat{\sigma}_{gv}$ (with $\hat{\sigma}_{gv} = |g\rangle\langle v|$) by expressing the $\hat{\sigma}$ operators in terms of their fluctuations $\delta\hat{\sigma}$ from their averages, i.e., $\hat{\sigma} = \langle\hat{\sigma}\rangle + \delta\hat{\sigma}$. This results in

$$\langle\hat{\rho}_{vv}\rangle = \langle(\langle\hat{\sigma}_{gv}^\dagger\rangle + \delta\hat{\sigma}_{gv}^\dagger)(\langle\hat{\sigma}_{gv}\rangle + \delta\hat{\sigma}_{gv})\rangle \quad (\text{F1})$$

$$= |\tilde{\rho}_{gv}|^2 + \langle\delta\hat{\sigma}_{gv}^\dagger \delta\hat{\sigma}_{gv}\rangle. \quad (\text{F2})$$

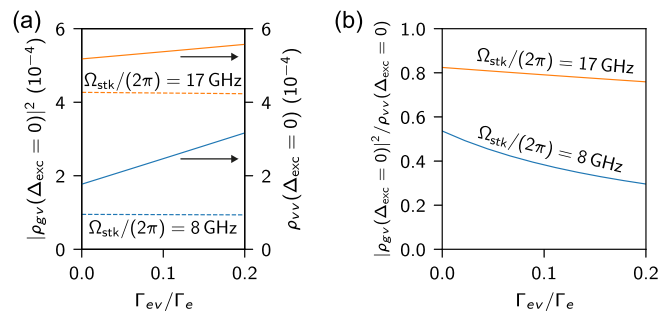


FIG. 11. Level of coherence in the population transferred to the vibronic state $|v\rangle$. (a) Total population (solid lines, right axis) and the level of the coherently transferred population (dashed lines, left axis) in level $|v\rangle$ predicted by the model of Fig. 7(a) and the parameters determined from the fit to the experimental data [shown in Fig. 4(a) of the main text] and $\Delta_{\text{exc}} = 0$. With an increasing fraction of spontaneous decay Γ_{ev}/Γ_e along $|e\rangle \rightarrow |v\rangle$, the fraction of coherently transferred population drops. (b) Fraction of the coherently transferred population in $|v\rangle$. For the maximum value of the Stokes laser Rabi frequency $\Omega_{\text{stk}}/(2\pi) = 17$ GHz achieved in the experiment of Fig. 4(a) in the main text, the model predicts that about 80% of the total population is coherent with the driving laser fields.

The first term of this equation ($\tilde{\rho}_{gv} = \langle\hat{\sigma}_{gv}^\dagger\rangle$) stands for the coherently transferred population, i.e. the part of the population that has a fixed phase relationship with respect to the (beat note of the) driving light fields. The latter part of the population has a randomized phase and is, thus, not coherent with the driving lasers.

Figure 11 shows the level of coherence transferred to $|v\rangle$ as predicted by the model of Fig. 7 and the parameters determined from a fit to the experimental data shown in Fig. 4(a) of the main text. Due to the fast vibrational relaxation rate of $|v\rangle$, the total population transferred to $|v\rangle$ is small with $\rho_{vv} \lesssim 10^{-3}$ [see Fig. 11(a)]. However, as shown in Fig. 11(a), the level of coherence in $|v\rangle$ is quite high for the highest value of the Rabi frequency achieved in the splitting measurements ($\Omega_{\text{stk}}/(2\pi) \approx 17$ GHz) and $\Delta_{\text{exc}} = 0$. This also holds if one takes the incoherent decay $|e\rangle \rightarrow |v\rangle$ at a rate Γ_{ev} into account. Figure 11(b) shows that the fraction of the coherent population in $|v\rangle$ is expected to be around 80% for the highest Stokes laser power ($P_{\text{stk}} = 2.65$ mW, corresponds to $\Omega_{\text{stk}}/(2\pi) \approx 17$ GHz) used in our experiments.

In Fig. 4(c) of the main text we assumed $\Gamma_{ev} = 0.01 \cdot \Gamma_{eg}$ (and then replaced $\Gamma_{eg} \rightarrow 0.99\Gamma_{eg}$) to estimate the level of coherence. Spontaneous decay $|e\rangle \rightarrow |v\rangle$ and incoherent vibrational relaxation from higher vibrational levels reduce the level of coherence, in particular if the Stokes laser is less intense and there is considerable excited state population. As discussed in the previous paragraph, this effect is not as relevant for the higher powers of the Stokes laser used in our experiment since in this case the Stokes laser-mediated population transfer is fast and the excited state population remains limited.

- [1] C. V. Raman, A new radiation, *Indian J. Phys.* **2**, 387 (1928).
- [2] C. V. Raman and K. S. Krishnan, A new type of secondary radiation, *Nature (London)* **121**, 501 (1928).
- [3] M. Aspelmeyer, T. J. Kippenberg, and F. Marquardt, Cavity optomechanics, *Rev. Mod. Phys.* **86**, 1391 (2014).
- [4] F. Benz, M. K. Schmidt, A. Dreismann, R. Chikkaraddy, Y. Zhang, A. Demetriadou, C. Carnegie, H. Ohadi, B. De Nijs, R. Esteban *et al.*, Single-molecule optomechanics in “picocavities”, *Science* **354**, 726 (2016).
- [5] S. T. Velez, K. Seibold, N. Kipfer, M. D. Anderson, V. Sudhir, and C. Galland, Preparation and decay of a single quantum of vibration at ambient conditions, *Phys. Rev. X* **9**, 041007 (2019).
- [6] A. Kudelski, Analytical applications of Raman spectroscopy, *Talanta* **76**, 1 (2008).
- [7] Q. Tu and C. Chang, Diagnostic applications of Raman spectroscopy, *Nanomedicine* **8**, 545 (2012).
- [8] S. Nie and S. R. Emory, Probing single molecules and single nanoparticles by surface-enhanced raman scattering, *Science* **275**, 1102 (1997).
- [9] K. Kneipp, Y. Wang, H. Kneipp, L. T. Perelman, I. Itzkan, R. R. Dasari, and M. S. Feld, Single molecule detection using surface-enhanced raman scattering (sers), *Phys. Rev. Lett.* **78**, 1667 (1997).
- [10] E. C. Le Ru and P. G. Etchegoin, Single-molecule surface-enhanced Raman spectroscopy, *Annu. Rev. Phys. Chem.* **63**, 65 (2012).
- [11] A. B. Zrimsek, N. Chiang, M. Mattei, S. Zaleski, M. O. McAnally, C. T. Chapman, A.-I. Henry, G. C. Schatz, and R. P. Van Duyne, Single-molecule chemistry with surface-and tip-enhanced Raman spectroscopy, *Chem. Rev.* **117**, 7583 (2017).
- [12] C. Zong, R. Premasiri, H. Lin, Y. Huang, C. Zhang, C. Yang, B. Ren, L. D. Ziegler, and J.-X. Cheng, Plasmon-enhanced stimulated raman scattering microscopy with single-molecule detection sensitivity, *Nat. Commun.* **10**, 5318 (2019).
- [13] H. Xiong, L. Shi, L. Wei, Y. Shen, R. Long, Z. Zhao, and W. Min, Stimulated Raman excited fluorescence spectroscopy and imaging, *Nat. Photon.* **13**, 412 (2019).
- [14] W. E. Moerner and L. Kador, Optical detection and spectroscopy of single molecules in a solid, *Phys. Rev. Lett.* **62**, 2535 (1989).
- [15] P. Tamarat, F. Jelezko, C. Brunel, A. Maali, B. Lounis, and M. Orrit, Non-linear optical response of single molecules, *Chem. Phys.* **245**, 121 (1999).
- [16] A. J. Maser, B. Gmeiner, T. Utikal, S. Götzinger, and V. Sandoghdar, Few-photon coherent nonlinear optics with a single molecule, *Nat. Photon.* **10**, 450 (2016).
- [17] C. Toninelli, I. Gerhardt, A. S. Clark, A. Reserbat-Plantey, S. Götzinger, Z. Ristanović, M. Colautti, P. Lombardi, K. D. Major, I. Deperasińska, W. H. P. Pernice, F. H. L. Koppens, B. Kozankiewicz, A. Gourdon, V. Sandoghdar, and M. Orrit, Single organic molecules for photonic quantum technologies, *Nat. Mater.* **20**, 1615 (2021).
- [18] S. Adhikari and M. Orrit, Progress and perspectives in single-molecule optical spectroscopy, *J. Chem. Phys.* **156**, 160903 (2022).
- [19] T. Plakhotnik, T. Nonn, and V. Palm, Saturation spectroscopy of vibronic transitions in single molecules, *Chem. Phys. Lett.* **357**, 397 (2002).
- [20] M. Banasiewicz, J. Dresner, O. Morawski, D. Wiacek, and B. Kozankiewicz, Purely electronic and vibronic fluorescence excitation of single terrylene molecules in a naphthalene crystal, *Acta Phys. Pol. A* **112**, S-85 (2007).
- [21] D. Wiacek and B. Kozankiewicz, Non-planar distortion of single molecules revealed by vibronic fluorescence excitation: Terrylene in p-terphenyl and naphthalene crystals, *Chem. Phys. Lett.* **462**, 280 (2008).
- [22] J. Zirkelbach, M. Mirzaei, I. Deperasińska, B. Kozankiewicz, B. Gurlek, A. Shkarin, T. Utikal, S. Götzinger, and V. Sandoghdar, High-resolution vibronic spectroscopy of a single molecule embedded in a crystal, *J. Chem. Phys.* **156**, 104301 (2022).
- [23] L. Shi, H. Xiong, Y. Shen, R. Long, L. Wei, and W. Min, Electronic resonant stimulated Raman scattering microspectroscopy, *J. Phys. Chem. B* **122**, 9218 (2018).
- [24] L. Wei and W. Min, Electronic preresonance stimulated Raman scattering microscopy, *J. Phys. Chem. Lett.* **9**, 4294 (2018).
- [25] S. Saikan, N. Hashimoto, T. Kushida, and K. Namba, Variation of inverse Raman spectrum near resonance, *J. Chem. Phys.* **82**, 5409 (1985).
- [26] L. Pei, X. Lu, J. Bai, X. Miao, R. Wang, L.-A. Wu, S. Ren, Z. Jiao, H. Zhu, P. Fu *et al.*, Resonant stimulated Raman gain and loss spectroscopy in rb atomic vapor, *Phys. Rev. A* **87**, 063822 (2013).
- [27] M. Fleischhauer, A. Imamoglu, and J. P. Marangos, Electromagnetically induced transparency: Optics in coherent media, *Rev. Mod. Phys.* **77**, 633 (2005).
- [28] A. Lazoudis, T. Kirova, E. H. Ahmed, L. Li, J. Qi, and A. M. Lyyra, Electromagnetically induced transparency in an open Λ -type molecular lithium system, *Phys. Rev. A* **82**, 023812 (2010).
- [29] E. H. Ahmed, J. Huennekens, T. Kirova, J. Qi, and A. M. Lyyra, The Autler–Townes effect in molecules: Observations, theory, and applications, in *Advances in Atomic, Molecular, and Optical Physics*, edited by P. Berman, E. Arimondo, and C. Lin (Academic Press, Cambridge, 2012), Vol. 61, pp. 467–514.
- [30] J. R. Hill, E. L. Chronister, T.-C. Chang, H. Kim, J. C. Postlewaite, and D. D. Dlott, Vibrational relaxation and vibrational cooling in low temperature molecular crystals, *J. Chem. Phys.* **88**, 949 (1988).
- [31] J. R. Hill, E. L. Chronister, T.-C. Chang, H. Kim, J. C. Postlewaite, and D. D. Dlott, Vibrational relaxation of guest and host in mixed molecular crystals, *J. Chem. Phys.* **88**, 2361 (1988).
- [32] S. Califano, V. Schettino, and N. Neto, *Lattice Dynamics of Molecular Crystals* (Springer, Berlin, Heidelberg, New York, 1981).
- [33] P. M. Anisimov, J. P. Dowling, and B. C. Sanders, Objectively discerning Autler–Townes splitting from electromagnetically induced transparency, *Phys. Rev. Lett.* **107**, 163604 (2011).
- [34] X. Lu, X. Miao, J. Bai, L. Pei, M. Wang, Y. Gao, L.-A. Wu, P. Fu, R. Wang, and Z. Zuo, Transition from Autler–Townes splitting to electromagnetically induced transparency based on the dynamics of decaying dressed states, *J. Phys. B* **48**, 055003 (2015).
- [35] L. Hao, Y. Jiao, Y. Xue, X. Han, S. Bai, J. Zhao, and G. Raitchel, Transition from electromagnetically induced transparency to

- Autler-Townes splitting in cold cesium atoms, *New J. Phys.* **20**, 073024 (2018).
- [36] N. R. Verhart, M. Müller, and M. Orrit, Spectroscopy of single dibenzoterrylene molecules in para-dichlorobenzene, *ChemPhysChem* **17**, 1524 (2016).
- [37] B. Gmeiner, A. Maser, T. Utikal, S. Götzinger, and V. Sandoghdar, Spectroscopy and microscopy of single molecules in nanoscopic channels: Spectral behavior vs. confinement depth, *Phys. Chem. Chem. Phys.* **18**, 19588 (2016).
- [38] R. J. Carlson and J. C. Wright, Analysis of vibrational correlations and couplings in the lowest two singlet states of pentacene by high resolution, fully resonant, coherent four-wave mixing spectroscopy, *J. Chem. Phys.* **92**, 5186 (1990).
- [39] K. K. Rebane and I. Rebane, Peak value of the cross-section of zero-phonon line's absorption, *J. Lumin.* **56**, 39 (1993).
- [40] C. Clear, R. C. Schofield, K. D. Major, J. Iles-Smith, A. S. Clark, and D. P. S. McCutcheon, Phonon-induced optical dephasing in single organic molecules, *Phys. Rev. Lett.* **124**, 153602 (2020).
- [41] M. Takayanagi, H.-O. Hamaguchi, and M. Tasumi, Probe-frequency dependence of the resonant inverse Raman band shape, *J. Chem. Phys.* **89**, 3945 (1988).
- [42] C. C. Tannoudji, J. Dupont-Roc, and G. Grynberg, *Atom-Photon Interactions: Basic Processes and Applications* (Wiley-VCH, Weinheim, 2004).
- [43] J. Qi, F. C. Spano, T. Kirova, A. Lazoudis, J. Magnes, L. Li, L. M. Narducci, R. W. Field, and A. M. Lyra, Measurement of transition dipole moments in lithium dimers using electromagnetically induced transparency, *Phys. Rev. Lett.* **88**, 173003 (2002).
- [44] E. Ahmed, A. Hansson, P. Qi, T. Kirova, A. Lazoudis, S. Kotochigova, A. Lyra, L. Li, J. Qi, and S. Magnier, Measurement of the electronic transition dipole moment by Autler-Townes splitting: Comparison of three- and four-level excitation schemes for the Na_2 $A^1\Sigma_u^+ - X^1\Sigma_g^+$ system, *J. Chem. Phys.* **124**, 084308 (2006).
- [45] S. Mukamel, *Principles of Nonlinear Optical Spectroscopy*, 6 (Oxford University Press, New York, 1995).
- [46] C. M. Tesch and R. de Vivie-Riedle, Quantum computation with vibrationally excited molecules, *Phys. Rev. Lett.* **89**, 157901 (2002).
- [47] S. Suzuki, K. Mishima, and K. Yamashita, Ab initio study of optimal control of ammonia molecular vibrational wavepackets: Towards molecular quantum computing, *Chem. Phys. Lett.* **410**, 358 (2005).
- [48] P. Roelli, C. Galland, N. Piro, and T. J. Kippenberg, Molecular cavity optomechanics as a theory of plasmon-enhanced Raman scattering, *Nat. Nanotechnol.* **11**, 164 (2016).
- [49] S. Bayliss, D. Laorenza, P. Mintun, B. Kovos, D. Freedman, and D. Awschalom, Optically addressable molecular spins for quantum information processing, *Science* **370**, 1309 (2020).
- [50] B. Gurlek, V. Sandoghdar, and D. Martín-Cano, Engineering long-lived vibrational states for an organic molecule, *Phys. Rev. Lett.* **127**, 123603 (2021).
- [51] K. Bergmann, N. V. Vitanov, and B. W. Shore, Perspective: Stimulated Raman adiabatic passage: The status after 25 years, *J. Chem. Phys.* **142**, 170901 (2015).
- [52] D. F. Phillips, A. Fleischhauer, A. Mair, R. L. Walsworth, and M. D. Lukin, Storage of light in atomic vapor, *Phys. Rev. Lett.* **86**, 783 (2001).
- [53] D. Höckel and O. Benson, Electromagnetically induced transparency in cesium vapor with probe pulses on the single-photon level, *Phys. Rev. Lett.* **105**, 153605 (2010).
- [54] M. Mücke, E. Figueroa, J. Bochmann, C. Hahn, K. Murr, S. Ritter, C. J. Villas-Boas, and G. Rempe, Electromagnetically induced transparency with single atoms in a cavity, *Nature (London)* **465**, 755 (2010).
- [55] H. P. Specht, C. Nölleke, A. Reiserer, M. Uphoff, E. Figueroa, S. Ritter, and G. Rempe, A single-atom quantum memory, *Nature (London)* **473**, 190 (2011).
- [56] L. Slodička, G. Hétet, S. Gerber, M. Hennrich, and R. Blatt, Electromagnetically induced transparency from a single atom in free space, *Phys. Rev. Lett.* **105**, 153604 (2010).
- [57] J. Zirkelbach, High-resolution spectroscopy of vibronic transitions in single molecules, Ph.D. thesis, Friedrich-Alexander Universität Erlangen-Nürnberg (2022).
- [58] T. Sharp and H. Rosenstock, Franck-Condon factors for polyatomic molecules, *J. Chem. Phys.* **41**, 3453 (1964).
- [59] V. Barone, J. Bloino, and M. Biczysko, Vibrationally-resolved electronic spectra in gaussian 09, Revision A 2, 1 (2009).
- [60] I. Deperasińska and B. Kozankiewicz (private communication).
- [61] M. Orrit, J. Bernard, and R. I. Personov, High-resolution spectroscopy of organic molecules in solids: From fluorescence line narrowing and hole burning to single molecule spectroscopy, *J. Phys. Chem.* **97**, 10256 (1993).
- [62] J. R. Johansson, P. D. Nation, and F. Nori, QuTiP: An open-source python framework for the dynamics of open quantum systems, *Comput. Phys. Commun.* **183**, 1760 (2012).
- [63] R. Fisher, Optimal control of multi-level quantum systems, Ph.D. thesis, Technische Universität München (2010).